

# Evaluating the Spatiotemporal Dynamics of Land Surface Temperature in Relation to the Land Use/Land Cover changes in Nag-Hammadi District, Egypt, using Remote Sensing and GIS

Mostafa K. Mosleh

Department of Geography, Faculty of Arts, South Valley University, Qena, 83523, Egypt

E-mail: dr.mostafak.mosleh@gmail.com

DOI: <https://doi.org/10.52939/ijg.v19i3.2599>

## Abstract

*In this study, three multi-temporal remotely sensed data acquired from Landsat-5 Thematic Mapper (TM) and Landsat -8 Operational Land Imager/Thermal Infrared Sensor (OLI/TIRS) in 1990, 2005, and 2020 were used. The maximum likelihood classifier (MLC) was opted to classify land use and land cover (LULC). Land surface temperature (LST) and LULC spectral indices i.e., Normalized Difference Vegetation Index (NDVI), Normalized Difference Built-up Index (NDBI), Normalized Difference Latent Heat Index (NDLI) and Bare Soil Index (BSI) have been computed and their relationships were examined. The overall accuracy of LULC was more than 93%. The analyses showed a notable transformation in LULC over the study period. For instance, built-up areas increased 103.7% with a rate of 45.5 ha/year and agriculture land increased by 28.9% with a rate of 186.4 ha/year. Whereas, bare soil was sharply decreased by 36.4% at a rate of 227.7ha/year. The minimum and maximum LST values increased by 2.9°C and 4.9°C, respectively, from 1990 to 2020. Furthermore, LST has a negative relationship with NDVI and NDLI (NDVI: 1990:  $r^2 = 0.62$ ; 2005:  $r^2 = 0.62$ ; 2020:  $r^2 = 0.65$ . NDLI: 1990:  $r^2 = 0.79$ ; 2005:  $r^2 = 0.78$ ; 2020:  $r^2 = 0.61$ ) and a positive relationship with NDBI and BSI (NDBI: 1990:  $r^2 = 0.68$ ; 2005:  $r^2 = 0.73$ ; 2020:  $r^2 = 0.44$ . BSI: 1990:  $r^2 = 0.77$ ; 2005:  $r^2 = 0.78$ ; 2020:  $r^2 = 0.53$ ). These results provided useful information about LULC changes and its impact on LST, which are necessary for experts and land-use planners to formulate sustainable LST mitigation policies, create an environmental comfort in Nag-Hammadi district, and other geographical locations with similar conditions.*

**Keywords:** Geospatial Mapping, GIS Analysis, LST, LULC, Spectral Indices

## 1. Introduction

The land use and land cover (LULC) rapidly changes due to various natural and anthropogenic activities. This promotes serious worldwide environmental and human concerns regarding energy balance, near-surface temperature over the cities and its surroundings, human comfort, physical health, and quality of life [1] [2] and [3]. In this context, land surface temperature (LST) is sensitive to LULC changes which, in turn, influences its spatial distribution and, as such, needs accurate monitoring [4] and [5]. Traditional ground field and in-situ methods for monitoring LULC and LST are costly, time-consuming, and involve a tedious process making the spatial analysis of LULC and LST difficult [6] and [7].

In this regard, geospatial technologies i.e., remote sensing and geographic information system (GIS) are effective for detecting the changes of

LULC and LST due to several reasons such as the low cost, availability, and large spatial coverage [8] and [9]. Several studies explored the impact of LULC changes on LST using GIS techniques and various satellite data over different geographical locations. Zhang et al., [10] used IKONOS data to obtain urban vegetation types and Landsat 7 Enhanced Thematic Mapper Plus (ETM+) thermal bands to retrieve LST over Nanjing City, China. They found that higher LST values are negatively correlated with the vegetation cover ( $r = -0.59$ ). The results also revealed greater cooling effect of large-vegetated areas over smaller ones. Mallick [11] applied ASTER image at 90m for mapping LULC and LST over semi-arid region of Abha, Kingdom of Saudi Arabia and found that the spatial distribution of LST was affected by LULC and negatively correlated with Normalized Difference

Vegetation Index (NDVI) with  $r^2$  value of 0.62. El-Zeiny and Effat [12] used Landsat Thematic Mapper (TM), ETM and Landsat 8 Operational Land Imager/Thermal Infrared Sensor (OLI/TIRS) images over El-Fayoum governorate, Egypt, and found that desert bare lands exhibited mean LST of  $>42^{\circ}\text{C}$  followed by urban areas, vegetation, and water bodies. Dhar et al., [13] utilized Landsat-5 TM, Landsat-8 OLI/TIRS, and Sentinel-2A for mapping LULC and estimating the LST over Rajarhat Block, West Bengal, India. The study showed an increase in LST to the tune of  $<1^{\circ}\text{C}$ . Furthermore, the results revealed negative correlation between NDVI and LST, whereas positive correlation occurred between Normalized Difference Built-up Index (NDBI) and LST of urban areas. Aik et al., [14] utilized Landsat 7 ETM+, Landsat 8 OLI/TIRS, and Moderate Resolution Imaging Spectroradiometer (MODIS) images over Cameron Highlands district, Malaysia. The results demonstrated that the measured LST showed a rise of about  $2\text{-}3^{\circ}\text{C}$  with an extreme of  $5^{\circ}\text{C}$  on average. The current study utilized Landsat

satellite images to evaluate the LULC changes and their impact on LST in Nag-Hammadi district over the past 30 years (1990 and 2020) as this region is the economic, commercial, agriculture and industrial hub in Upper Egypt. The specific objectives of this study are to (i) analyze the spatiotemporal changes of LULC over the last three decades from 1990 to 2020; (ii) analyze the spatiotemporal variation of LST, and (iii) evaluate the relationship between LST and selected LULC spectral indices.

## 2. Study Area

Geographically, Nag-Hammadi district is located in Upper Egypt between  $25^{\circ}26'18''$  to  $26^{\circ}08'58''$  N latitude and  $32^{\circ}09'47''$  to  $32^{\circ}27'03''$  E longitude (**Figure 1**). The district belongs to Qena governorate with a total area of 40703.58 hectare (ha). The population increased from 373504 in 1996 to 451891 in 2006 and reached 578237 in 2017 [15]. Climatologically, it is characterized by a desert climate i.e., hot, and dry summer and warm winter.

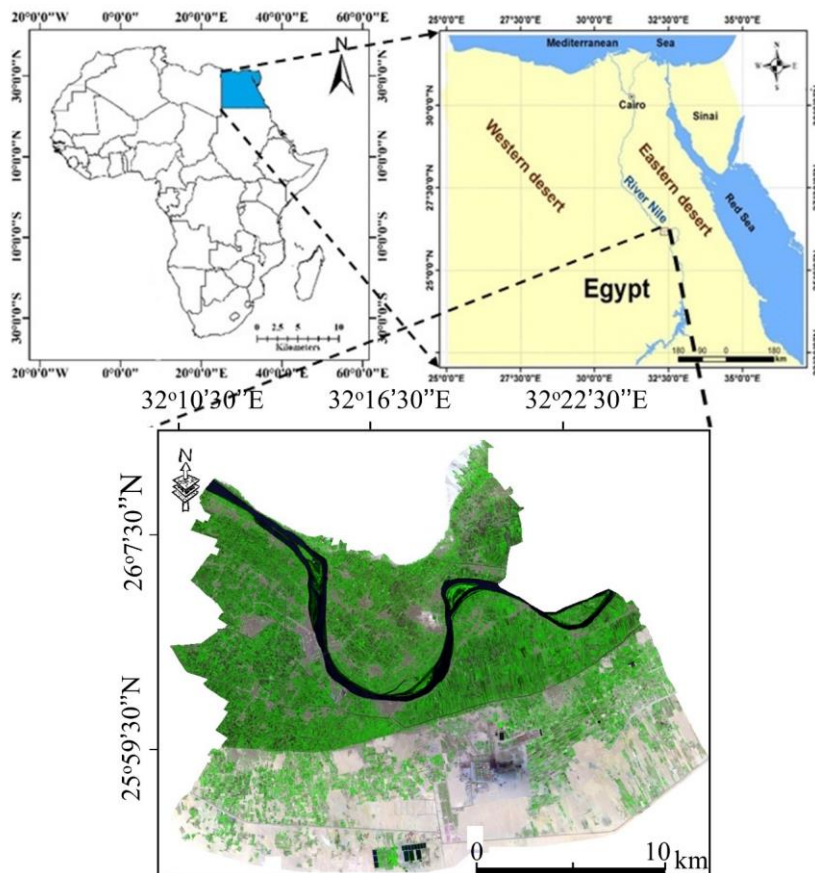


**Figure 1:** Geographical location of the study area (Nag-Hammadi district)

In the summer, the average maximum temperature is 44°C, while it is 24°C in the winter. The maximum relative humidity is 53% in the winter and 29% in the summer. It rarely rains [16]. Agriculture is the prime source of livelihood for the population, and it's cultivated with various fruits, vegetables, and field crops depending on the irrigation from the Nile River and underground sources. In addition, the district is home to the largest factory of aluminium production in the Middle East, and the largest factory for sugar production in Egypt.

### 3. Materials and Methods

**Figure 2** shows the conceptual diagram of the major procedures adopted in this study.

#### 3.1 Data Collection and Pre-Processing

Remotely sensed surface reflectance and surface temperature imageries from Landsat 5 and Landsat 8 were used for the LULC classification and the LST estimation of Nag-Hammadi district. Three satellite images from the Landsat series i.e., Landsat-5 for 1990, 2005, and Landsat 8 OLI/TIRS for 2020 were freely acquired from the United States Geological Survey (USGS) (<https://earthexplorer.usgs.gov>). These images were

selected in June and July to avoid the seasonal variation of climatic conditions with cloud-free status peering in mind that the LST and its relation to LULC is maximize in the summer. **Table 1** provides a descriptive summary of the Landsat imageries that have been used in this study. Only band 10 from Landsat 8 was used for retrieving LST because band 11 is affected by stray light and ghosting issues and faced calibration uncertainty [14]. All the used spectral bands were stacked and clipped to the boundary of the study area. Furthermore, other auxiliary datasets such as topographic maps at scale (1: 50,000), land use maps and high spatial resolution images from Google Earth were used to support the analysis. In this context, several band combinations of the Landsat images were tested to generate different composite effects and increase the interpretation of LULC. A combination of NIR, red, and green spectral bands were used in displaying the RGB color composite image for Landsat 5 TM and Landsat 8. Then, four LULC classes were visually identified namely: built-up area, agricultural land, water bodies, and bare soil and verified from the field investigation.

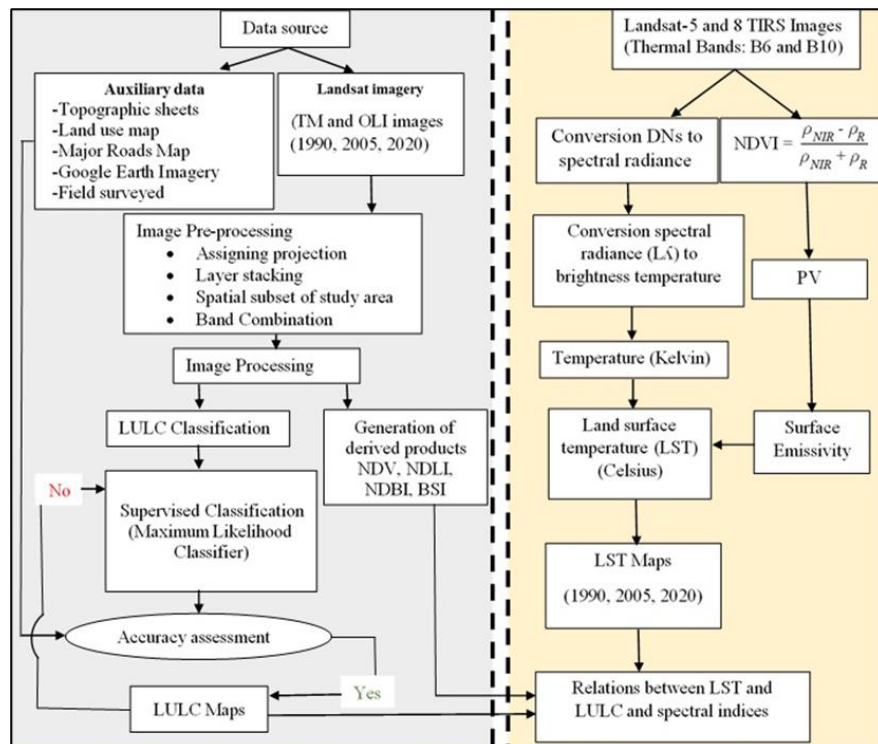


**Figure 2:** Conceptual diagram of the adopted methodology, (a) generation of LULC maps and derived-based indices, (b) derivation of LST and its relation with LULC and spectral indices

**Table 1:** Description of the satellite imagery used for LST and LULC in this study

| Type of Satellite | Sensor ID                                                        | Path/Row | Date of acquisition            | Band Name and Wavelength (µm)                   | Spatial Resolution (m) |
|-------------------|------------------------------------------------------------------|----------|--------------------------------|-------------------------------------------------|------------------------|
| Landsat – 5       | Thematic Mapper (TM)                                             | 175/42   | June 10, 1990;<br>July 5, 2005 | Band 1_Blue: 0.45–0.52                          | 30                     |
|                   |                                                                  |          |                                | Band 2_Green: 0.52–0.60                         | 30                     |
|                   |                                                                  |          |                                | Band 3_Red: 0.63–0.69                           | 30                     |
|                   |                                                                  |          |                                | Band 4_Near Infrared (NIR): 0.76–0.90           | 30                     |
|                   |                                                                  |          |                                | Band 5_Shortwave Infrared (SWIR-1): 1.55–1.75   | 30                     |
|                   |                                                                  |          |                                | Band 6_TIR(Thermal): 10.40-12.50                | 120*                   |
|                   |                                                                  |          |                                | Band 7_Shortwave Infrared (SWIR-2): 2.08–2.35   | 30                     |
| Landsat –8        | Operational Land Imager (OLI) and Thermal Infrared Sensor (TIRS) | 175/42   | June 12, 2020                  | Band 2_Blue: 0.45 – 0.51                        | 30                     |
|                   |                                                                  |          |                                | Band 3_Gerrn: 0.53 – 0.59                       | 30                     |
|                   |                                                                  |          |                                | Band 4_Red: 0.64 – 0.67                         | 30                     |
|                   |                                                                  |          |                                | Band 5_Near Infrared (NIR): 0.85 – 0.88         | 30                     |
|                   |                                                                  |          |                                | Band 6_Shortwave Infrared (SWIR-1): 1.57 – 1.65 | 30                     |
|                   |                                                                  |          |                                | Band 7_Shortwave Infrared (SWIR-2): 2.11–2.29   | 30                     |
|                   |                                                                  |          |                                | Band 10 Thermal Infrared (TIRS-1) 10.60–11.19   | 100*                   |

\* Resampled to 30 m pixels by USGS from the original 120 and 100m resolution.

Built-up areas represent Naj-Hammadi city, all rural villages, commercial and industrial buildings, and transportation facilities. Agricultural land includes all cultivated lands with field crops, vegetables or fruit trees, and harvested lands. Water bodies include the Nile River, irrigation, and drainage canals. Bare soil includes uncultivated land or land with no vegetation cover.

### 3.2 Image Classification

Supervise-based maximum likelihood classifier (MLC) was employed to classify the Landsat images. MLC is robust and requires less extended training process, and it is commonly used for the precise monitoring and assessment of the LULC changes [11] [12] and [17]. In this study, the training sets were drawn using the on-screen digitizing for each of the LULC types for each image. This allows for generating spectral signatures for the LULC classes which were input into the MLC algorithm. Then, accuracy assessment was performed using four hundred (400) reference sample points computed based on binomial probability theory using equation 1 and spatially distributed using a stratified random schema to represent the four LULC classes located in the study area. The binomial probability theory can be represented as follows:

$$N = \frac{z^2 \times p \times q}{E^2} \quad \text{Equation 1}$$

where:

$N$  = Sample size

$p$  = Expected percent accuracy of the entire map

$q = 100-p$

$E$  = Allowable error

$z = 2$

Then, for each image the overall, user's, and producer's accuracies and Kappa coefficient were calculated for the classified images using equations 2-5:

$$\text{Overall Accuracy (\%)} = \frac{\sum \text{Diagonal Value}}{N} \times 100 \quad \text{Equation 2}$$

where: Diagonal value = Number of correctly classified pixels for each class:

$N$  = Total number of pixels (reference samples)

$$\text{User's Accuracy (\%)} = \frac{\text{Diagonal Value of Row}}{\text{Row Total}} \times 100 \quad \text{Equation 3}$$

$$\text{Producer's Accuracy (\%)} = \frac{\text{Diagonal Value of Column}}{\text{Column Total}} \times 100 \quad \text{Equation 4}$$

$$K = \frac{N \sum_{i=1}^r x_{ii} - \sum_{i=1}^r (x_{i+} \times x_{+i})}{N^2 - \sum_{i=1}^r (x_{i+} \times x_{+i})} \quad \text{Equation 5}$$

where:

$K$  = Kappa coefficient

$r$  = Number of rows in the matrix

$x_{ii}$  = Number of observations in row  $i$  and column  $i$

$x_{i+}$  and  $x_{+i}$  = Marginal sum of row  $i$  and column  $i$  respectively

$N$  = Total number of observations (pixels) in the entire matrix

As a role of thumb if the accuracy of the classified image is greater than 85% and Kappa statistic is above 0.75 then it would be acceptable for LULC classification [18]. Finally, the magnitude of the change (MC), the percentage of change (PC), and the annual rate of change (ARC) were computed to determine the changes in LULC during the study periods using equations 6-8 [19]:

$$MC (ha) = A_i - A_f \quad \text{Equation 6}$$

$$PC(\%) = \frac{A_i - A_f}{A_i} \times 100 \quad \text{Equation 7}$$

$$ARC(ha/year) = \left( \frac{A_i - A_f}{n} \right) \quad \text{Equation 8}$$

where:  $A_i$  = Class area (ha) at the initial time

$A_f$  = Class area (ha) at the final time

$n$  = Number of years of the time period

### 3.3 Calculation of LULC Spectral Indices

Four common spectral indices were used to monitor LULC and LST. The NDVI (equation 9; [20]) values range from -1 to 1 where higher NDVI values indicate dense vegetation cover while lower values (typically from 0 to 0.2) indicate non-vegetated cover [21]. The NDBI (equation 10) is sensitive to the built-up features and has been promoted as an effective measure to identify built-up areas using the short-wave infrared and the near-infrared regions of the spectrum [1] [4] and [22]. The values of NDBI range from -1 to 1. The higher values represent high density built-up areas, whereas lower values refer to vegetation or water. The Normalized Difference Latent Heat Index (NDLI, equation 11) has been proven to be an effective indicator for monitoring water content using a combination of the three spectral bands (i.e., green, red, SWIR) due to their spectral response to water content from other land cover types [23] [24] and [25]. The NDLI values greater than 0 to 1 indicate existence of water content. The Bare Soil

Index (BSI) has been utilized for monitoring and mapping the bare soil areas using equation 12 [26] and [27] where the higher value denotes bare soil. Equations 9-12 are expressed as follow:

$$NDVI = \frac{NIR - RED}{NIR + RED} \quad \text{Equation 9}$$

$$NDBI = \frac{SWIR - NIR}{SWIR + NIR} \quad \text{Equation 10}$$

$$NDLI = \frac{GREEN - RED}{GREEN + RED + SWIR} \quad \text{Equation 11}$$

$$BSI = \frac{(SWIR1 + RED) - (NIR + BLUE)}{(SWIR1 + RED) + (NIR + BLUE)} \quad \text{Equation 12}$$

where:

$NIR$  = Near infrared band (i.e., 0.76-0.90  $\mu\text{m}$  for Landsat TM and 0.85-0.88  $\mu\text{m}$  for Landsat-8 OLI)

$RED$  = Red band (i.e., 0.63-0.69  $\mu\text{m}$  for Landsat TM and 0.64-0.67  $\mu\text{m}$  for Landsat-8 OLI)

$SWIR1$  = Shortwave infrared band (i.e., 1.55-1.75  $\mu\text{m}$  for Landsat TM and 1.57-1.65  $\mu\text{m}$  for Landsat-8 OLI)

$GREEN$  = Green spectral band (i.e., 0.52-0.60  $\mu\text{m}$  for Landsat TM and 0.53-0.59  $\mu\text{m}$  for Landsat-8 OLI)

$BLUE$  = Blue band (i.e., 0.45-0.52  $\mu\text{m}$  for the Landsat TM and 0.45-0.51  $\mu\text{m}$  for Landsat-8 OLI)

### 3.4 Retrieving LST

To retrieve LST from thermal band of Landsat imageries the following procedures are explained below.

#### 3.4.1 Conversion of digital number (DN) values to top-of-atmosphere (TOP) spectral radiance ( $L\lambda$ )

The calculation of the spectral radiance ( $L\lambda$ ) has been done using the rescaling factors provided in the metadata file [28] using equation 13 for Landsat-5 TM imageries for years 1990-2005 and equation 14 for Landsat-8 TIRS band for the year of 2020. Equation 13 is presented as follow:

$$L\lambda = \left[ \frac{L_{MAX.\lambda} - L_{MIN.\lambda}}{Q_{CAL.MAX} - Q_{CAL.MIN}} \right] \times (Q_{CAL} - Q_{CALMIN}) + L_{MIN.\lambda} \quad \text{Equation 13}$$

where:

$L\lambda$  = Spectral radiance at sensor's aperture in  $\text{w}/(\text{m}^2 \cdot \text{sr} \cdot \mu\text{m})$

$L_{MAX,\lambda}$  = Spectral radiance scaled to  $Q_{CAL,MAX}$  i.e., DN value 255

$L_{MIN,\lambda}$  = Spectral radiance scaled to  $Q_{CAL,MIN}$  i.e., DN value 1

$Q_{CAL}$  = Pixel values of satellite images (DN)

$Q_{CAL,MAX}$  = Quantized and calibrated maximum pixel value (corresponding to  $L_{MAX,\lambda}$ )

$Q_{CAL,MIN}$  = Quantized and calibrated minimum pixel value (corresponding to  $L_{MIN,\lambda}$ )

Equation 14 is expressed as follow:

$$L_{\lambda} = M_L \times Q_{CAL} + A_L \quad \text{Equation 14}$$

where:

$M_L$  = Multiplicative rescaling factor for the radiance of the specific spectral band (n) obtained from the metadata of the dataset (i.e., RADIANCE\_MULT\_BAND\_n)

$A_L$  = Additive rescaling factor for the radiance of the spectral band (n) retrieved from the metadata of the image's dataset (i.e., RADIANCE\_ADD\_BAND\_n)

### 3.4.2 Conversion of spectral radiance to brightness temperature (in Kelvin)

The spectral radiance was converted to brightness temperature ( $T_B$ ) in Kelvin using equation 15, then it was converted from kelvin ( $^{\circ}K$ ) to degree Celsius ( $^{\circ}C$ ) using equation 16:

$$T_B = \frac{K_2}{\ln\left(\frac{K_1}{L_{\lambda}} + 1\right)} \quad \text{Equation 15}$$

$$T_{B(^{\circ}C)} = T_{B(\text{in kelvin})} - 273.15 \quad \text{Equation 16}$$

where:

$T_B$  = At satellite brightness temperature in Kelvin

$L_{\lambda}$  = TOA spectral radiance  $w/(m^2 \cdot sr \cdot \mu m)$

$K_1$  and  $K_2$  = Two pre-launch calibration constants of thermal bands obtained from the image's metadata

For Landsat-5, value of  $K_1$  for band 6 is 607.76 and  $K_2$  for band 6 is 1260.56, and for Landsat-8, value of  $K_1$  for band 10 is 774.8853 and  $K_2$  for band 10 is 1321.0789.

### 3.4.3 Calculating of proportion of vegetation ( $P_v$ )

Proportion of vegetation ( $P_v$ ) retrieved using equation 17:

$$P_v = \left( \frac{NDVI - NDVI_{min}}{NDVI_{max} - NDVI_{min}} \right)^2 \quad \text{Equation 17}$$

where:

$NDVI$  = Normalised Difference Vegetation Index as computed using equation 9 for each of the years

$NDVI_{min}$  = Minimum value of NDVI for that year

$NDVI_{max}$  = Maximum value of NDVI for that year

### 3.4.4 Estimation of the land surface emissivity (LSE)

The Land surface emissivity (LSE ( $\epsilon$ )) is an essential parameter to estimate the LST. It was computed using equation 18:

$$\text{Surface emissivity}(\epsilon) = (0.004 \times P_v) + 0.986 \quad \text{Equation 18}$$

### 3.4.5 Estimation of LST

After retrieving the emissivity images for each year, the LST was derived using equation 19:

$$LST(^{\circ}C) = \frac{T_B}{1 + \left[ \left( \lambda \times \frac{T_B}{\rho} \right) \times \ln(\epsilon) \right]} \quad \text{Equation 19}$$

where:

$T_B$  = At sensor brightness temperature

$\lambda$  = Wavelength of emitted radiance (i.e., the average wavelengths = 10.8  $\mu m$ )

$\rho = h \times \left( \frac{c}{\sigma} \right) = 1.438 \times 10^{-2} \text{ m} \cdot \text{K}$  ( $h$  = Planck's constant ( $6.626 \times 10^{-34} \text{ J} \cdot \text{s}$ ))

$c$  = Velocity of light at a vacuum ( $2.998 \times 10^8 \text{ m/s}$ )

$\sigma$  = Boltzmann constant ( $1.38 \times 10^{-23} \text{ J/K}$ )

$\epsilon$  = Land surface emissivity (LSE)

LST was then classified into appropriate and color-coded ranges to produce a thermal pattern distribution map for Nag-Hammada district.

### 3.5 Correlation and Regression Analysis

The analyses of the relationships between the LULC spectral indices and LST for each year were evaluated using linear regression analysis at the pixel level. A hundred randomly selected sample points (pixels) from LST, NDVI, NDBI, NDLI and BSI images within the study area for each study period were employed to evaluate the relationship using the coefficient of determination  $r^2$ , equation 20:

$$r^2 = \left( \frac{\sum_{i=1}^n (x_i - \bar{x})(y_i - \bar{y})}{\sqrt{\sum_{i=1}^n (x_i - \bar{x})^2} \sqrt{\sum_{i=1}^n (y_i - \bar{y})^2}} \right)^2 \quad \text{Equation 20}$$

where:

$x_i$  = Independent variable of NDVI, NDBI, NDLI and BSI measuring value of  $x_i$

$y_i$  = Dependent variable of LST measuring value of  $y_i$

$n$  = Number of observations

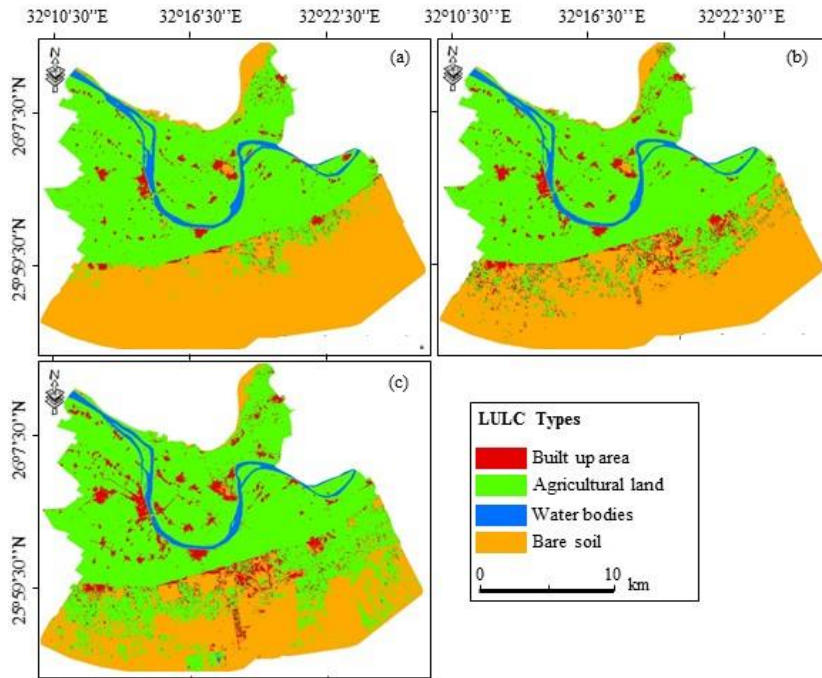


**Figure 3:** Geographical distributions of spatio-temporal LULC changes in Naj Hammadi district for the years (a) 1990, (b) 2005, and (c) 2020

**Table 2:** Area coverage for each land cover class (Hectares) and percentage of LULC classes

| LULC Classes      | 1990     |        | 2005     |        | 2020     |        |
|-------------------|----------|--------|----------|--------|----------|--------|
|                   | Area(ha) | %      | Area(ha) | %      | Area(ha) | %      |
| Built-up area     | 1316.07  | 3.2    | 2136.82  | 5.2    | 2680.63  | 6.6    |
| Agricultural land | 19293.93 | 47.4   | 21084.3  | 51.8   | 24884.64 | 61.1   |
| Water bodies      | 1300.59  | 3.2    | 1247.58  | 3.1    | 1176.66  | 2.9    |
| Bare soil         | 18792.99 | 46.2   | 16234.88 | 39.9   | 11961.65 | 29.4   |
| Total             | 40703.58 | 100.00 | 40703.58 | 100.00 | 40703.58 | 100.00 |

## 4. Results and Discussion

### 4.1 LULC changes from 1990 to 2020

The spatiotemporal analysis of LULC changes is presented in **Figure 3(a) to (c)** and **Table 2**. Results showed that the agricultural land was dominant during the period of interest and experienced gradual increase from 47.4% to 61.1% of the study area. The built-up area increased from 3.2% to 6.6%, while the bare soil and water bodies were declined from 46.2 to 29.4% and from 3.2 to 2.9% from 1990 to 2020, respectively. **Table 3** shows the MC of the LULC classes between the years. During period one, between 1990 - 2005, the study shows a noticeable decrease of -2558.11 ha with a change difference of -6.3% for the bare soil class. Water bodies observed an MC of -53.01 ha with a change difference of -0.1%. Whereas, the agricultural land witnessed an increase in MC of +1790.37 ha, with a change difference of 4.4%. The built-up area demonstrated an increase in MC of +820.75 ha with

differences change of 2%. In the second period, between 2005 - 2020, bare soil class had witnessed a decline of -4273.23 ha with a change difference of -10.5%. Water bodies observed an MC of -70.92 ha with a change difference of -0.2%. On the contrary, agricultural land witnessed an increase of +3800.34 ha with a change difference of +9.3%. Furthermore, the built-up area witnessed an increase of +543.81 ha with a change difference of +1.4%. Additionally, the land cover distribution demonstrated various change between 1990 - 2020. The bare soil and water bodies witnessed a loss of -6831.34 ha (-16.8%) and -123.93 ha (-0.3%), respectively. Land coverage by agricultural land and built-up area witnessed the highest increase with +5590.71 ha (+13.7%) and +1364.56 ha (+3.4%), respectively. The analysis of the MC and PC remarkably show that the increase of built-up areas was at expense of bare soil and agricultural lands.

This increase would be related to the population growth, which has contributed to massive human activities and development. Moreover, it can be observed that agricultural lands were increased in line with the decrease of bare soil and maintain its domination over the entire study period. Such increasing trend in agriculture lands exists mainly towards the southern side of the study area.

This would be due to the continuous investment in agricultural activities (i.e., new land reclamation) over the past thirty years in the study area which significantly contributed to the alteration of LULC types. **Figure 4** shows the annual rate of change (ARC) of the LULC in three different periods (1990 – 2005; 2005 – 2020 and 1990 – 2020). In the first period, a significant annual increase in the built-up area (54.7 ha/year) was mostly occurred at the expense of agricultural and bare soil (-170.5). Slight annual increase and decrease were observed in the agricultural land and water bodies; 119.4 ha/year and -3.5 ha/year, respectively. During the second period the annual increase in built-up areas with rate of 36.3 ha/year, and agricultural land increased with a rate of 253.4 ha/year, which occurred on expense of the bare soil (-284.9 ha/year). During the entire study period (i.e., 1990-2020) agricultural land was the largest land cover in the region with annual increase of 186.4 ha/year. The built-up area

witnessed an increase of 45.5 ha/year. While, both water bodies and bare soil decreased by annual rate of -4.1 and 227.7 ha/year, respectively. It was observed that this increase was synchronized with a decrease in the bare soil during the whole period of study which might be a reflection of the governmental developmental projects (i.e., urban development and fringe desert reclamation).

#### 4.2 Accuracy Assessment

The overall accuracies of the classified LULC maps were 93.25%, 94.5% and 96.25%, for the 1990, 2005, and 2020, respectively, which is satisfactory given that an accuracy of 80% is a minimum criterion [18]. Kappa values were 0.91, 0.93, and 0.95, respectively for the same years indicated for acceptable classification. The accuracy assessment for each LULC class is summarized in **Tables 4-6**. In all of the classified maps, the water bodies class had the highest user's and producer's accuracies due to its distinct spectral signature from the other LULC classes. Also, slightly low errors were observed between built-up area and agriculture land classes which would likely be due to their distinct spectral confusion. Moreover, the color reflection resemblance of the roofs of the traditional buildings and paved roads in the study area could mistakenly be classified across other land uses [29].

**Table 3:** The magnitude of the change (MC) in land cover classes between years

| LULC Classes      | 1990-2005        |         | 2005-2020        |          | 1990-2020        |          |
|-------------------|------------------|---------|------------------|----------|------------------|----------|
|                   | Area change (ha) | % Diff  | Area change (ha) | % Diff   | Area change (ha) | % Diff   |
| Built-up area     | (+)820.75        | (+) 2   | (+) 543.81       | (+) 1.4  | (+) 1364.56      | (+) 3.4  |
| Agricultural land | (+)1790.37       | (+) 4.4 | (+) 3800.34      | (+) 9.3  | (+) 5590.71      | (+) 13.7 |
| Water bodies      | (-) 53.01        | (-) 0.1 | (-) 70.92        | (-) 0.2  | (-) 123.93       | (-) 0.3  |
| Bare soil         | (-)2558.11       | (-) 6.3 | (-) 4273.23      | (-) 10.5 | (-) 6831.34      | (-) 16.8 |

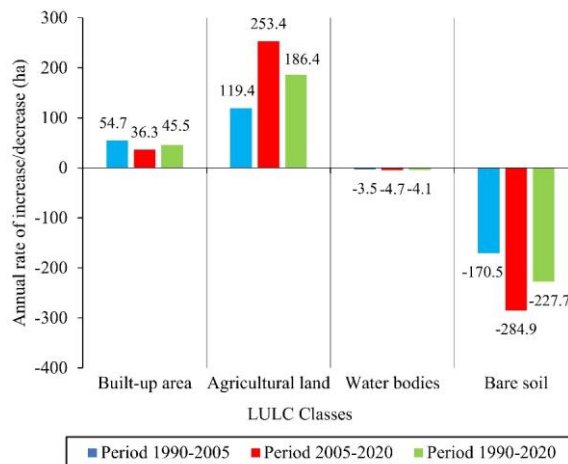


**Figure 4:** Graph showing annual rate of change for each LULC classes (ha/year) during the period of study

#### 4.3 Land Surface Temperature Change (LSTC)

**Figure 5** shows the spatial distributions of LST retrieved from satellite images for the three study periods (1990, 2005 and 2020). It shows the variation of the minimum and maximum LST across Nag-Hammadi district which ranges between 21.94°C and 49.57°C in 1990. In 2005, the LST values varied between 24.12°C and 45.57°C, while in 2020, the LST values were within the range of 24.84°C to 54.56 which revealed an increase in the minimum and maximum LST over the last three decades by approximately of 2.9°C and 4.98°C, respectively. This increase in the LST values could

be attributed to the increasing built-up areas and other impervious surface in the study area from 1990 to 2020.

#### 4.4 Variation of LST for Different LULC Types

**Figure 6** summarizes the mean values of LST (°C) of each LULC type during the three years of interest 1990, 2005 and 2020. Zonal statistics analysis was performed to summarize the relationship between LULC and LST. The comparison between the LST and LULC map indicated low mean values of about 23°C, 25°C, and 26 °C in water bodies in 1990, 2005, and 2020, respectively.

**Table 4:** Confusion matrix of 1990 classified LULC map

| LULC-Category       | Built-up | Agricultural | Water | Bare soil | Total | User's accuracy | Kappa coefficient |
|---------------------|----------|--------------|-------|-----------|-------|-----------------|-------------------|
| Built-up area       | 88       | 3            | 1     | 5         | 97    | 90.7            | 0.91              |
| Agricultural land   | 5        | 95           | 2     | 2         | 104   | 91.3            |                   |
| Water bodies        | 0        | 2            | 98    | 0         | 100   | 98              |                   |
| Bare soil           | 4        | 3            | 0     | 92        | 99    | 92.9            |                   |
| Total               | 97       | 103          | 101   | 99        | 400   |                 |                   |
| Producer's accuracy | 90.7     | 92.2         | 97    | 92.9      |       |                 |                   |
| Overall accuracy    | 93.25    |              |       |           |       |                 |                   |

**Table 5:** Confusion matrix of 2005 classified LULC map

| LULC-Category       | Built-up | Agricultural | Water | Bare soil | Total | User's accuracy | Kappa coefficient |
|---------------------|----------|--------------|-------|-----------|-------|-----------------|-------------------|
| Built-up area       | 85       | 3            | 1     | 4         | 93    | 91.4            | 0.93              |
| Agricultural land   | 2        | 97           | 2     | 4         | 105   | 92.4            |                   |
| Water bodies        | 0        | 3            | 96    | 0         | 99    | 96.9            |                   |
| Bare soil           | 2        | 1            | 0     | 100       | 103   | 97.1            |                   |
| Total               | 89       | 104          | 99    | 108       | 400   |                 |                   |
| Producer's accuracy | 95.5     | 93.3         | 97    | 92.6      |       |                 |                   |
| Overall accuracy    | 94.5     |              |       |           |       |                 |                   |

**Table 6:** Confusion matrix of 2020 classified LULC map.

| LULC-Category       | Built-up | Agricultural | Water | Bare soil | Total | User's accuracy | Kappa coefficient |
|---------------------|----------|--------------|-------|-----------|-------|-----------------|-------------------|
| Built-up area       | 98       | 1            | 0     | 4         | 103   | 95.2            | 0.95              |
| Agricultural land   | 4        | 96           | 0     | 2         | 102   | 94.1            |                   |
| Water bodies        | 0        | 1            | 99    | 0         | 100   | 99              |                   |
| Bare soil           | 2        | 1            | 0     | 92        | 95    | 96.8            |                   |
| Total               | 104      | 99           | 99    | 98        | 400   |                 |                   |
| Producer's accuracy | 94.2     | 96.9         | 100   | 93.9      |       |                 |                   |
| Overall accuracy    | 96.25    |              |       |           |       |                 |                   |

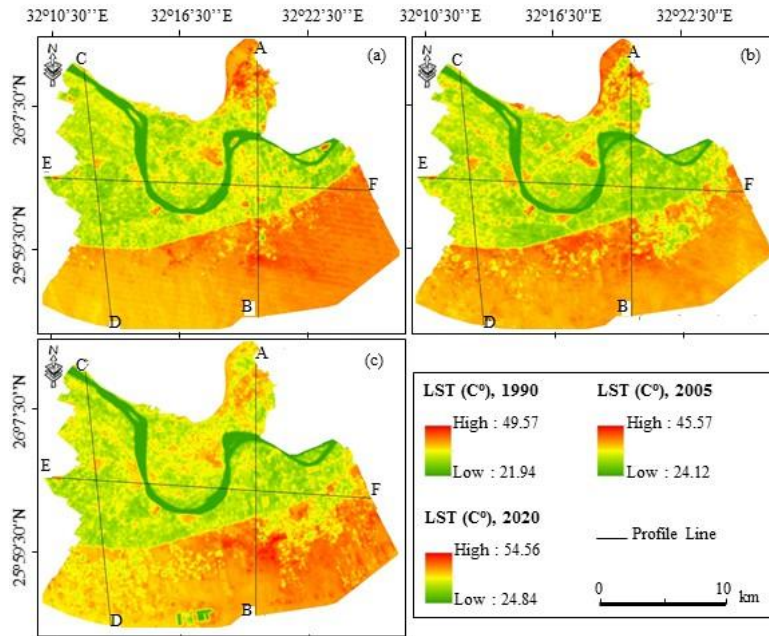


**Figure 5:** Spatial distribution of LST in Naj-Hammadi district in (a) 1990; (b) 2005; and (c) 2020. A-B, C-D and E-F represent LST spatial profiles as shown in Figure 7

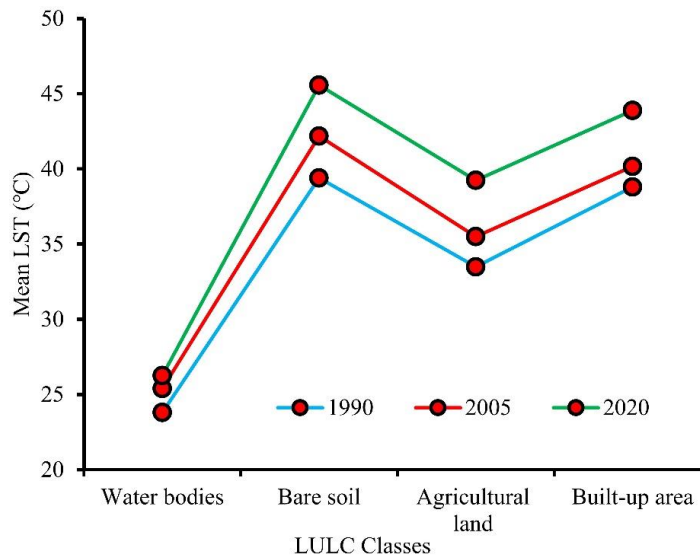


**Figure 6:** Temporal distribution of mean LST (°C) over LULC types in 1990, 2005 and 2020

While high mean values of 38°C, 40°C, and 43°C in built-up area and 39°C, 42°C, and 45°C in bare soil in 1990, 2005, and 2020, respectively. This indicates that urban areas contribute on rising LST on the account of other LULC as the urban areas are mainly constructed from impervious surfaces such as stone, metal, and concrete which exhibit low evaporation. Meanwhile, the bare soils exhibit higher LST values according to the diurnal cycle variation of LST.

The agricultural lands show moderate LST values in all years due to the evapotranspiration and vegetation density. To deepen the understanding of the impact of LULC changes on LST, three arbitrary cross sections were created across the study area to represent the LULC types wise LST. These included two cross-sections (i.e., A-B, C-D) from north to south and E-F from west to east (Figure 7).

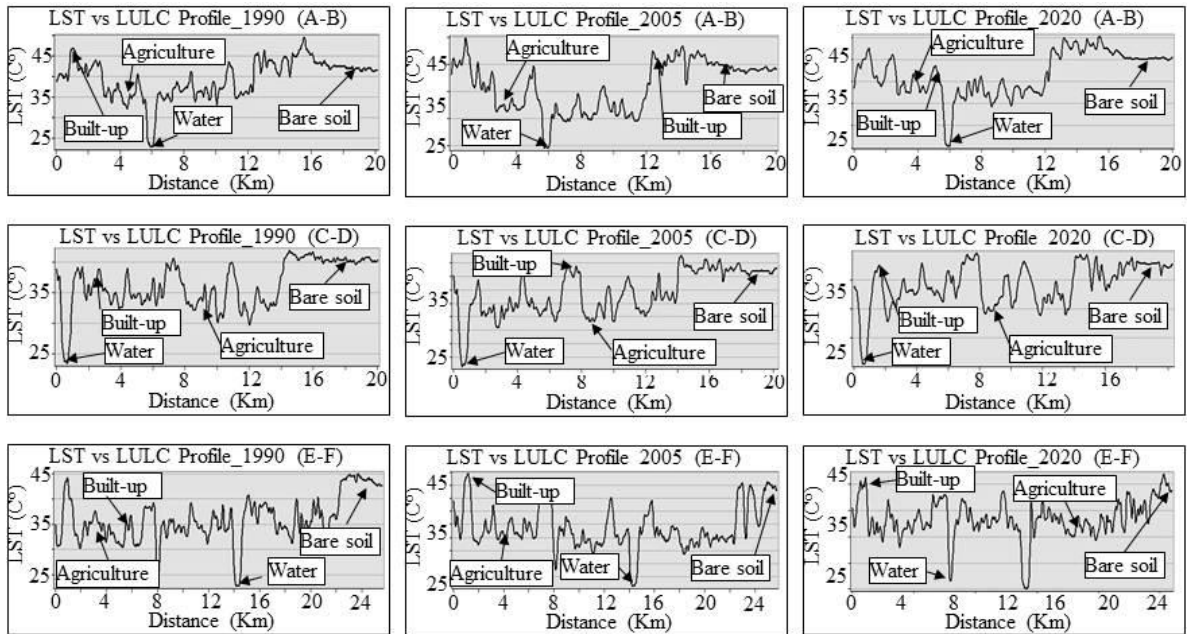


**Figure 7:** LST versus LULC profiles for the spatial profiles shown in Figure 5 for the years 1990, 2005, and 2020

It is seen from the cross profiles that bare soil exhibits highest LST with  $\sim 45^{\circ}\text{C}$  followed by built-up area  $\sim 40^{\circ}\text{C}$ . In three different cross-sections, the water bodies and agricultural land showed the lower LST of  $\sim 22^{\circ}\text{C}$  and  $\sim 34^{\circ}\text{C}$ , respectively, in 1990. The LST values for bare soil, built-up area, water bodies, and agricultural land were  $\sim 40^{\circ}\text{C}$ ,  $\sim 42^{\circ}\text{C}$ ,  $\sim 23^{\circ}\text{C}$  and  $\sim 34^{\circ}\text{C}$ , respectively in 2005. In 2020, these values were  $\sim 46^{\circ}\text{C}$ ,  $\sim 44^{\circ}\text{C}$ ,  $\sim 25^{\circ}\text{C}$  and  $\sim 37^{\circ}\text{C}$ , respectively. From the analysis, it can be inferred that agricultural lands shows low LST in all years due to the heat reduction within vegetation cover due to its density and transpiration. These outcomes conform to the findings of different studies [30] and [31].

#### 4.5 Relationship between LST with LULC Spectral Indices

**Figure 8** shows the spatial distribution of NDVI values derived using Landsat images of 1990, 2005 and 2020. The results showed that the NDVI values ranged between -0.50 and 0.72 in 1990, while it was -0.41 and 0.69 in 2005, and -0.19 and 0.57 in 2020. These results demonstrate the highest NDVI values in the east and west banks along the Nile River within Nag-Hammadi district, which mainly is covered by densely vegetated areas (i.e., most productive agricultural land) leading to lower LST. The distribution of NDVI values of Nag-Hammadi district in 1990, 2005, and 2020 is presented in **Figure 9**. The results demonstrated that the NDVI

values ranged between -0.09 to 0.17 in 1990. This was -0.12 and 0.09 in 2005 as well as -0.08 and 0.08 in 2020. The NDVI values were low in built-up areas and bare soils and high in the water bodies and vegetation cover which is consistent with other studies such as [25].

The NDBI (**Figure 10**) values ranged between -0.51 to 0.36 in 1990. In 2005, these values were between -0.49 and 0.44 as well as -0.39 and 0.28 in 2020. The NDBI values were very high in the built-up areas and bare soils as they are exposed to the incoming solar radiation. Finally, the spatial distribution of BSI values in 1990, 2005, and 2020 is presented in **Figure 11**. The result demonstrates that the BSI values ranged between -0.54 and 0.13 in 1990, -0.46 and 0.14 in 2005, and -0.30 and 0.19 in 2020. Among them, the bare soils have the highest BSI value. **Figures 12 and 13** illustrate the results of the relationship between LST and LULC spectral indices. The linear regression analysis demonstrates that higher LST were corresponding to areas of low vegetation cover and vice-versa. In this study, the statistical analysis and scatter plots clearly shows that the LST is negatively correlated to NDVI; having a coefficient of determination  $R^2$  value of 0.62 in 1990, 0.62 in 2005, and 0.65 in 2020. The result of the correlation and regression analysis discloses a positive correlation between NDBI-derived built-up areas and LST with  $R^2$  values of 0.68 in 1990, 0.73 in 2005, and 0.44 in 2020 (**Figure 12**).

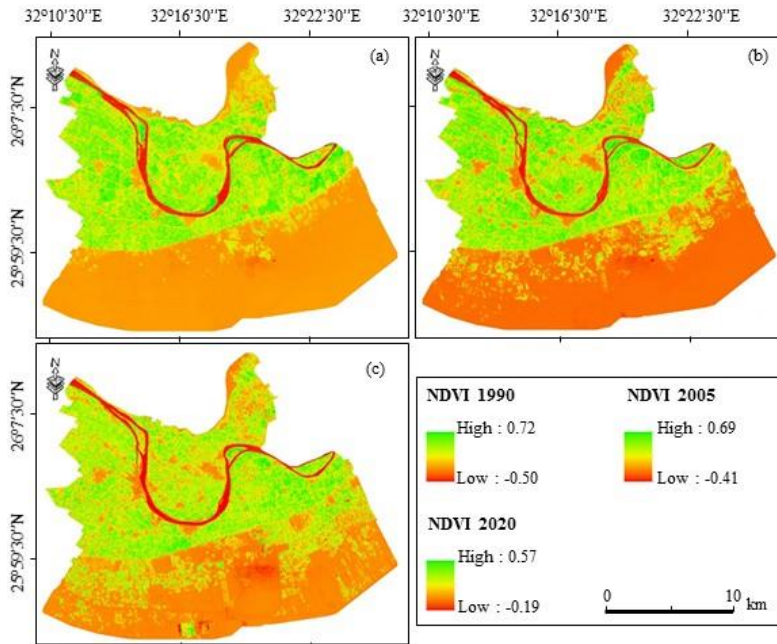


**Figure 8:** Spatial distribution of NDVI in Naj-Hammadi district in (a) 1991; (b) 2005; and (c) 2020

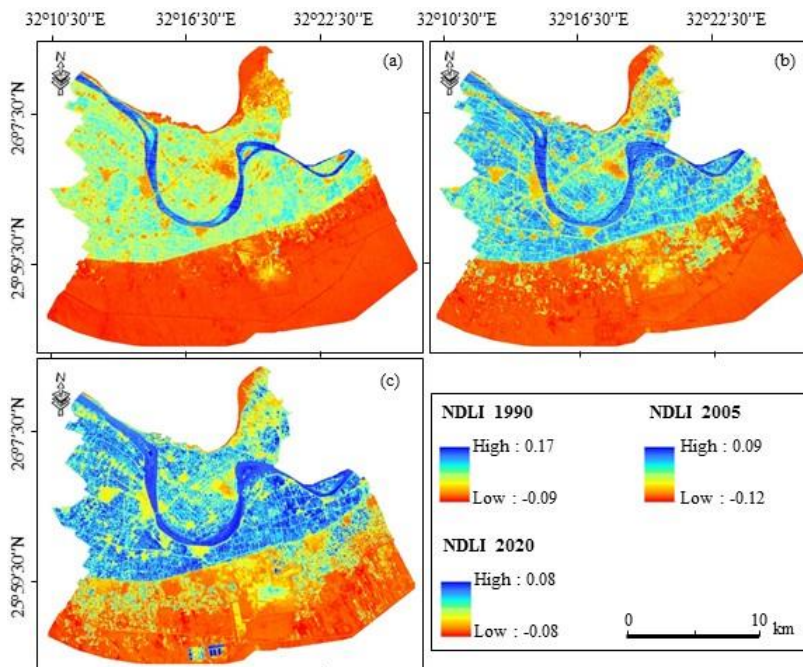


**Figure 9:** Spatial distribution of NDLI in Naj-Hammadi district in (a) 1990; (b) 2005; and (c) 2020

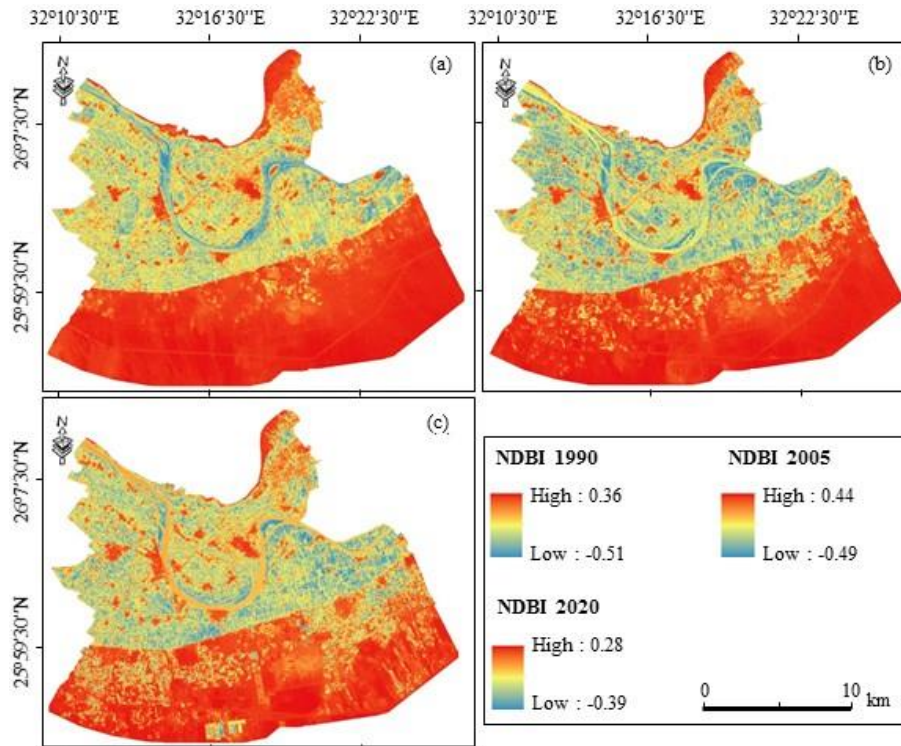


**Figure 10:** Spatial distribution of NDBI in Naj-Hammadi district in (a) 1990; (b) 2005; and (c) 2020

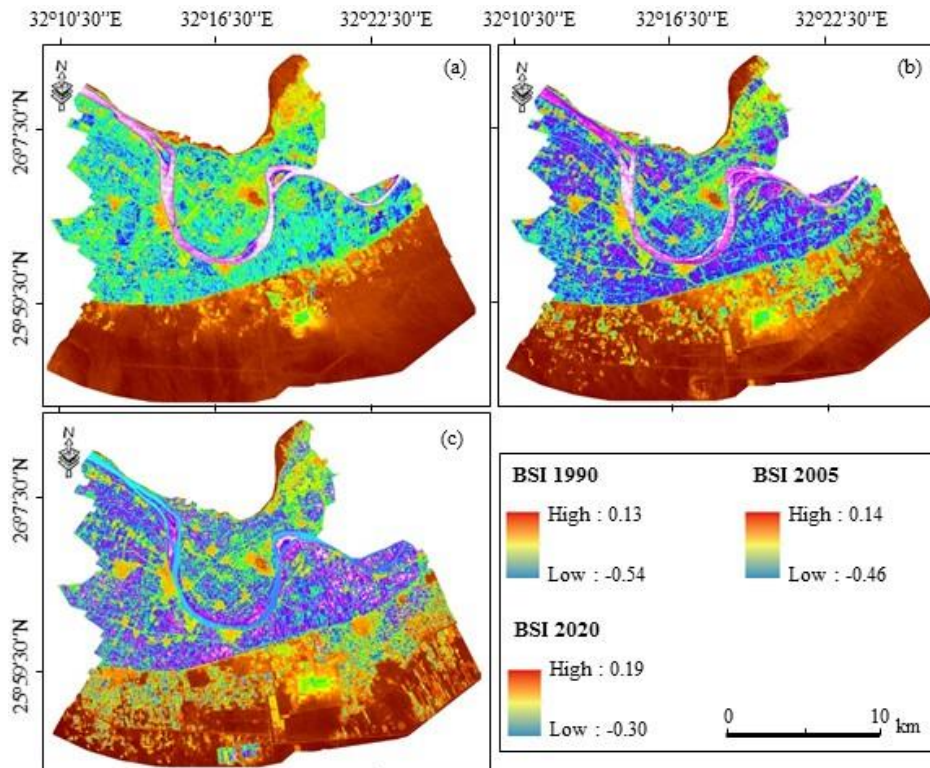


**Figure 11:** Spatial distribution of BSI in Naj-Hammadi district in (a) 1990; (b) 2005; and (c) 2020

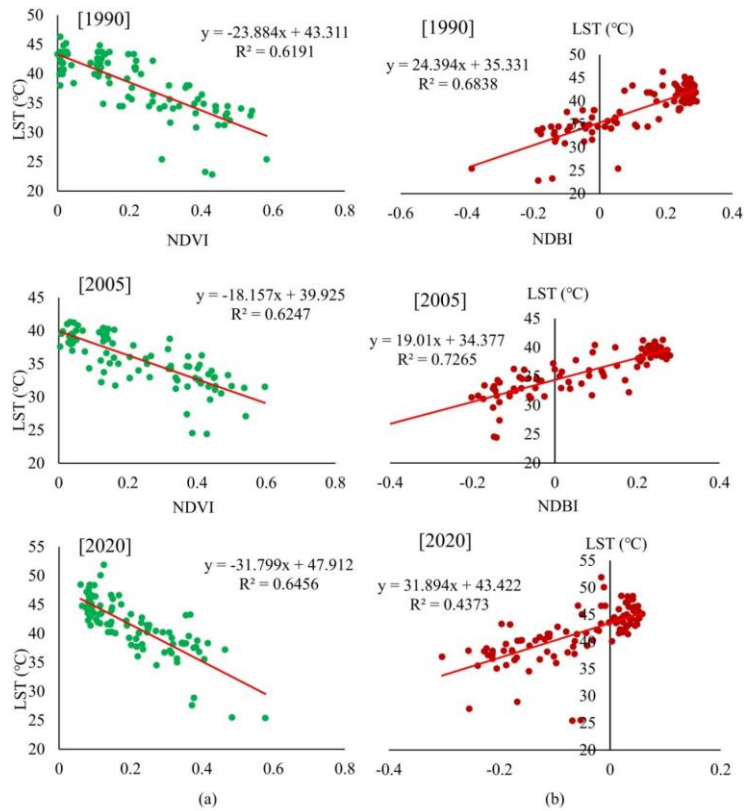


**Figure 12:** Graph showing scatter plot for (a) LST and NDVI; (b) LST and NDBI

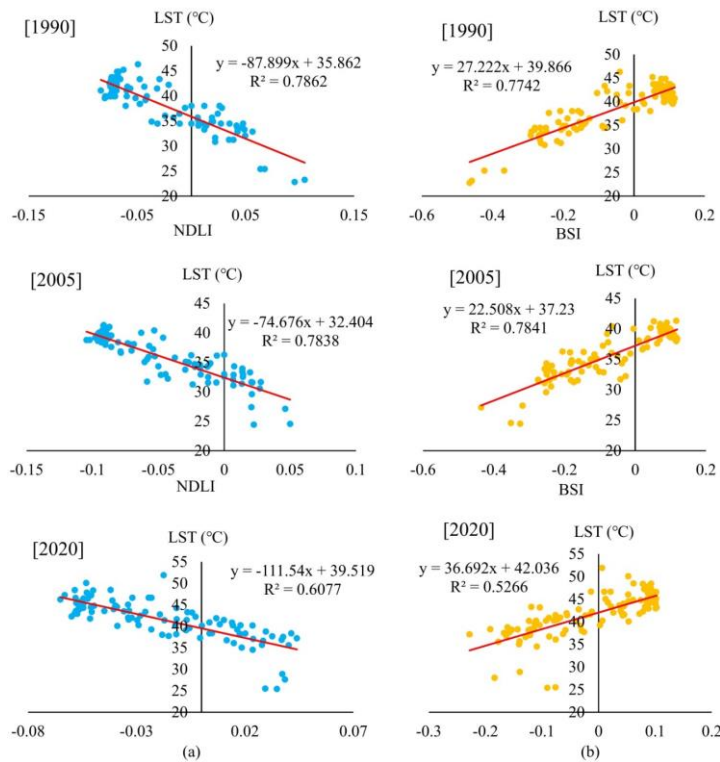


**Figure 13:** Graph showing scatter plot for (a) LST and NDLI; (b) LST and BSI

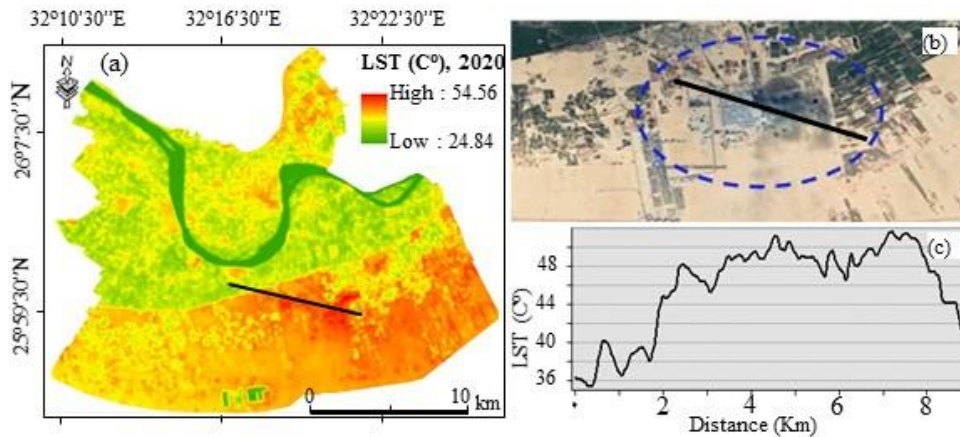


**Figure 14:** (a) Spatial distribution of LST in Naj-Hammadi district in 2020, (b) true colour image of the Aluminium factory area, and (c) spatial profile of LST detected for the Aluminium factory area

This denotes that the lower the NDBI, the lower the LST while the higher NDBI indicates a higher LST. The results show a negative correlation between NDVI-derived water features and LST due to the physical changes, increased moisture in the irrigated areas, and profusion of vegetation, which influence the heating of the ground surface [32]. The coefficient of determination shows  $R^2$  values of 0.79 in 1990, 0.78 in 2005, and 0.61 in 2020 (**Figure 13**). Also, the low LST values in vegetated areas would be due to the processes of transpiration and evapotranspiration [33]. On top of that, the negative correlation between the NDVI and LST are due to evapotranspiration process which reduces the surface temperature. Thus, the findings of this study are closely consistent with recent studies such as [24].

Further to examine the changes in bare soil lands, BSI maps of 1990, 2005, and 2020 were produced. The result reveals a positive correlation between BSI-derived bare soil and LST with  $R^2$  values of 0.77 in 1990, 0.78 in 2005, and 0.53 in 2020 (**Figure 13**). This relationship would be attributed to the low evaporation and low heat transfer capacity. Similar findings were reported in other studies such as [1] [25] [34] [35] [36] and [37].

It is noteworthy to mention that the study area is the home of heavy industries (i.e., Aluminium and Sugar factories), which is accountable for a notable increase in the surface temperature with LST value of 54°C by ~5-7°C compared to its surroundings. The LST profile across the industrial area also confirmed the existence of this case in this area (**Figure 14**).

## 5. Conclusion

The study effectively explored the changes in LULC and their impacts on LST in Nag-Hammadi district, Upper Egypt from 1990-2020, using geospatial technologies. The results indicated a significant increase in built-up area and agriculture lands, while bare soil and water bodies declined which subsequently affect the LST within the study area. The relationship between LST and LULC spectral indices was examined and interpreted quantitatively by linear regression analysis at the pixel level. The regression analysis showed that vegetated areas (NDVI) and water bodies (NDLI) have a negative relationship with LST, and positive relationship in the built-up areas (i.e., NDBI) and bare soil (i.e., BSI). Some of vital causes behind the higher surface temperature in built-up areas might be due to the urban growth and development in the socio-economic activities, which affected the radiative properties in the study area. These findings would be valuable for local government authorities and decision makers since they provide the updated information of LULC dynamics, improve understanding and identification of areas that have a higher LST to implement long-term sustainable strategies to mitigate the effect of LST and create a friendly environment in the study area for a sustainable future.

## Acknowledgements

The Author would like to express thankful to the United States Geological Survey (USGS) for assisting this research with datasets. The author is grateful to the anonymous reviewers for their constructive comments and suggestions to improve the manuscript.

## References

- [1] Balew, A. and Korme, T., (2020). Monitoring Land Surface Temperature in Bahir Dar City and its Surrounding using Landsat Images. *Egypt. J. Remote Sens. Space Sci.*, Vol. 23(3), 371–386. <https://doi.org/10.1016/j.ejrs.2020.02.001>.
- [2] Wesley, E. J. and Brunsell, N. A., (2019). Greenspace Pattern and the Surface Urban Heat Island: A Biophysically-Based Approach to Investigating the Effects of Urban Landscape Configuration. *Remote Sens.*, Vol. 11(19). <https://doi.org/10.3390/rs11192322>.
- [3] Grover, A. and Singh, R. B., (2016). Monitoring Spatial Patterns of Land Surface Temperature and Urban Heat Island for Sustainable Megacity: A Case Study of Mumbai, India, using Landsat TM Data. *Environ. Urban. Asia.*, Vol. 7(1), 38-54. <http://dx.doi.org/10.1177/0975425315619722>.
- [4] Dai, Z., Guldmann, J. M. and Hu, Y., (2018). Spatial Regression Models of Park and Land-Use Impacts on the Urban Heat Island in Central Beijing. *Sci. Total. Environ.*, Vol. 626(1), 1136–1147. <https://doi.org/10.1016/j.scitotenv.2018.01.165>
- [5] Malik, M. S., Shukla, J. P. and Mishra, S., (2019). Relationship of LST, NDBI and NDVI using Landsat-8 in Kandaihimmat Watershed, Hoshangabad, India. *Indian J. Mar. Sci.*, Vol. 48(01), 25-31.
- [6] Chaudhary, B. S., Saroha, G. P. and Yadav, M., (2008). Human Induced Land Use/Land Cover changes in Northern Part of Guragon District, Haryana, India. *J. Hum. Ecol.*, Vol. 23(3), 243-252. <https://doi.org/10.1080/09709274.2008.11906077>.
- [7] Shen, H., Huang, L., Zhang, L., Wu, P. and Zeng, C., (2016). Long-Term and Fine-Scale Satellite Monitoring of the Urban Heat Island Effect by the Fusion of Multi-Temporal and Multi-Sensor Remote Sensed Data: A 26-Year Case Study of the City of Wuhan in China. *Remote Sens. Environ.*, Vol. 172, 109–125. <http://dx.doi.org/10.1016/j.rse.2015.11.005>
- [8] Li, M., Zang, S., Zhang, B., Li, S. and Wu, C., (2014). A Review of Remote Sensing Image Classification Techniques: The Role of Spatio-Contextual Information. *Eur. J. Remote Sens.*, Vol. 47(1), 389-411. <https://doi.org/10.5721/EuJRS.20144723>
- [9] Dissanayake, D., (2020). Land Use Change and Its Impacts on Land Surface Temperature in Galle City, Sri Lanka. *Clim.*, Vol. 8(5). <https://doi.org/10.3390/cli8050065>
- [10] Zhang, X., Zhong T., Feng X. and Wang, K., (2009). Estimation of Relationship between Vegetation Patches and Urban Land Surface Temperature with Remote Sensing. *Int. J. Remote Sens.*, Vol. 30(8), 2105-2118. <https://doi.org/10.1080/01431160802549252>.
- [11] Mallick, J., (2014). Land Characterization Analysis of Surface Temperature of Semi-Arid Mountainous City Abha, Saudi Arabia using Remote Sensing and GIS. *J. Geogr. Inf. Syst.*, Vol.6(6), 664-676. <https://doi.org/10.4236/jgis.2014.66055>.
- [12] El-Zeiny, A. M. and Effat, H. A., (2017). Environmental Monitoring of Spatiotemporal Change in Land Use/Land Cover and Its Impact on Land Surface Temperature in El-Fayoum Governorate, Egypt. *Remote Sens. Appl. Soc. Environ.*, Vol. 8, 266-277. <https://doi.org/10.1016/j.rsase.2017.10.003>.
- [13] Dhar, R. B., Chakraborty, S., Chattopadhyay, R. and Sikdar, P. K., (2019). Impact of Land Use/Land Cover Change on Land Surface Temperature using Satellite Data: A Case Study of Rajarha Block, North 24-Parganas District, West Bengal. *J. Indian Soc. Remote Sens.*, Vol. 47(4), 331-348.
- [14] Aik, D. H. J., Ismail, M. H. and Muharam, F. M., (2020). Land Use/Land Cover Changes and the Relationship with Land Surface Temperature using Landsat and MODIS Imageries in Cameron Highlands, Malaysia. *Land.*, Vol. 9(10). <https://doi.org/10.3390/land9100372>.
- [15] CAPMAS., (1996, 2006 and 2017). *General Census of Population, Housing and Establishment*. Central Agency for Public Mobilization and Statistics, Cairo, Egypt.
- [16] Egyptian Metrological Authority. (2020). *Annual and Monthly Meteorological Report*. Cairo, Egypt.
- [17] Lillesand, T. M. and Kiefer, R. W., (1994). *Remote Sensing and Photo Interpretation*, (3rd Ed). John Wiley and Sons, New York.
- [18] Anderson, R., Hardy, E. E., Roach, J. T., Witmer, R. E. and Peck, D. L., (1976). *A Land Use and Land Cover Classification System for use with Remote Sensor Data*. U. S. Geological Survey Professional Paper, 964, Washington, DC. USA.
- [19] Alawamy, J. S., Balasundram, S. K., Hanif, A. H. M. and Sung, C. T. B., (2020). Detecting and Analyzing Land Use and Land Cover Changes in the Region of Al-Jabal Al-Akhdar, Libya using Time-Series Landsat Data from 1985 to 2017.

- Sustain.*, Vol. 12 (11). <https://doi.org/10.3390/su12114490>.
- [20] Rouse, J. W., Hass, R. H., Schell, J. A. and Deering, D. W., (1973). Monitoring Vegetation Systems in the Great Plains with ERTS. *Proceedings of the Third ERTS Symposium*, Washington, DC, USA. 309–317.
- [21] Barbieri, T., Despini, F. and Teggi, S., (2018). A Multi-Temporal Analyses of Land Surface Temperature Using Landsat-8 Data and Open Source Software: The Case Study of Modena, Italy. *Sustain.*, Vol. 10(5). <https://doi.org/10.3390/su10051678>.
- [22] Zha, Y., Gao, J. and Ni, S., (2003). Use of Normalized Difference Built-Up Index in Automatically Mapping Urban Areas from TM Imagery. *Int. J. Remote Sens.*, Vol. 24(3), 583–594.
- [23] Liou, Y., Le, M. S. and Chien, H., (2019). Normalized Difference Latent Heat Index for Remote Sensing of Land Surface Energy Fluxes. *IEEE Trans Geosci. Remote Sens.*, Vol. 57(3), 1423-1433. <https://doi.org/10.1109/TGRS.2018.2866555>.
- [24] Liou, Y. and Mulualem, G. M., (2019). Spatio-Temporal Assessment of Drought in Ethiopia and the Impact of Recent Intense Droughts. *Remote Sens.*, Vol. 11(15). <https://doi.org/10.3390/rs11151828>.
- [25] Traore, M., Lee, M. S., Rasul, A. and Balew, A., (2021). Assessment of Land Use/Land Cover Changes and their Impacts on Land Surface Temperature in Bangui (The Capital of Central African Republic). *Environ. Chall.*, Vol. 4. <https://doi.org/10.1016/j.envc.2021.100114>.
- [26] Mzid, N., Pignatte, S., Huang, W., and Casa, R., (2021). An Analysis of Bare Soil Occurrence in Arable Croplands for Remote Sensing Topsoil Applications. *Remote Sens.*, Vol. 13(3). <https://doi.org/10.3390/rs13030474>.
- [27] Elfadaly, A., Wafa, O., Abouarab, M. A. R., Guida, A., Spanu, P. G. and Lasaponara, R., (2017). Geo-Environmental Estimation of Land Use Changes and Its Effect on Egyptian Temples at Luxor City. *Int. J. Geo. Inf.*, Vol. 6(11). <https://doi.org/10.3390/ijgi6110378>.
- [28] Smith, R. B., Bonneau, L., Lee, X., Woo, L. and Fein, F., (2013). *Guide to Landsat 8 Image Processing*. The Yale Center for Earth Observation: Yale University, CT, USA, 1-8.
- [29] Fitawok, M. B., Derudder, B., Minale, A. S., Passel, S., Adgo, E. and Nyssen, J., (2020). Modeling the Impact of Urbanization on Land-Use Change in Bahir Dar City, Ethiopia: An Integrated Cellular Automata-Markov Chain Approach. *Land.*, Vol. 9(4). <https://doi.org/10.3390/land9040115>.
- [30] Pal, S. and Ziaul, S., (2017). Detection of Land Use and Land Cover Change and Land Surface Temperature in English Bazar Urban Centre. *Egypt. J. Remote Sens. Space Sci.*, Vol. 20(1), 125-145. <https://doi.org/10.1016/j.ejrs.2016.11.003>.
- [31] Al Kafy, A., Al-Faisal, A., Hasan, M. M., Sikdar, M., Khan, M. H. H., Rahman, M. and Islam, R., (2019). Impact of LULC Changes on LST in Rajshahi District of Bangladesh: A Remote Sensing Approach. *J. Geogr. Stud.*, Vol. 3(1), 11-23.
- [32] Ibrahim, G. R. F., (2017). Urban Land Use Land Cover changes and their Effect on Land Surface Temperature: Case Study using Dohuk City in the Kurdistan Region of Iraq. *Clim.*, Vol. 5(1). <https://doi.org/10.3390/cli5010013>.
- [33] Hanamean, J. R., Pielke, Sr. R. A., Castro, C. L., Ojima, D. S., Reed, B. C. and Gao, Z., (2003). Vegetation Greenness Impacts on Maximum and Minimum Temperatures in Northeast Colorado. *Meteorol. Appl.*, Vol. 10(3), 203-215. <https://doi.org/10.1017/S135048270303013>.
- [34] Su, Y. F., Foody, G. M. and Cheng, K., (2012). Spatial Non-Stationarity in the Relationships between Land Cover and Surface Temperature in Urban Heat Island and Its Impacts on Thermally Sensitive Populations. *Landsc. Urban Plan.*, Vol. 107(2), 172–180.
- [35] Ahmed, H. A., Singh, S. K., Kumar, M., Maina, M. S., Dzwairo, R. and La, L. D., (2020). Impact of Urbanization and Land Cover Change on Urban Climate: Case Study of Nigeria. *Urban Clim.*, Vol. 32. <https://doi.org/10.1016/j.uclim.2020.100600>.
- [36] Tan, J., Yu, D., Li, Q., Tan, X. and Zhou, W., (2020). Spatial Relationship Between Land-Use/Land-Cover Change and Land Surface Temperature in the Dongting Lake Area, China. *Sci. Rep.*, Vol. 10(1). <https://doi.org/10.1038/s41598-020-66168-6>.
- [37] Imran, H.M., Hossain, A., Islam, A.K.M.S., Rahman, A., Bhuiyan, M.A.E., Paul, S. and Alam, A., (2021). Impact of Land Cover Changes on Land Surface Temperature and Human Thermal Comfort in Dhaka City of Bangladesh. *Earth Syst. Environ.*, Vol. 5(11), 667–693. <https://doi.org/10.1007/s41748-021-00243-4>.